

Isospaced linear ion strings

Michael Johanning¹

Received: 30 July 2015 / Accepted: 20 January 2016 / Published online: 23 March 2016
© Springer-Verlag Berlin Heidelberg 2016

Abstract We describe the static and dynamical properties of strings of ions stored in segmented electrodynamic Paul traps with a uniform ion separation. In this work, this specific ion arrangement is achieved by a smooth anharmonic effective potential generated by suitable voltages applied to segmented dc electrodes or by appropriate electrode shaping. We find analytic expressions for the required field, potential and normal mode matrix and find that even finite systems closely reproduce the critical radial binding strength of an infinite size system at the transition from linear to zigzag configuration. From the normal mode matrix, we find that such strings exhibit a solid-state-like band of normal modes and determine the effective spin–spin coupling when the ion string is exposed to a magnetic gradient. We show how the potential, modes and couplings can be altered while still maintaining a homogeneous spacing and present numerical examples, for how this potential can be achieved in either segmented Paul traps or by using an optimized electrode geometry.

1 Introduction

In quantum information science (QIS) with cold trapped ions, there are many situations where a linear chain of trapped ions is preferential [1–3]. A linear string of ions provides a scalable quantum register where ions interact

and can be manipulated individually with low crosstalk [4–9]. Combining single ion addressability in anharmonic traps with conditional gates based on transverse modes allows for a large-scale quantum processor utilizing such a register [10]. Such a quantum processor will be particularly useful as part of a quantum repeater where a long-lived quantum memory and multi-qubit gates are necessary ingredients. If suitable quantum repeaters are used, the maximum distance for quantum communication scales with the size and coherence time of the quantum memory [11–13].

Other applications of long linear ion strings might involve, among others:

- *Quantum simulations* already a range of physical systems, not necessarily 1-d, can be simulated in a linear ion trap-based quantum simulator [14–19]. The effective spin–spin interactions might be tuned by the methods described here or by exploiting transverse modes [20]; when, for example, investigating the Frenkel Kontorova model with anharmonic trapping, the competition of the trapping potential and an additional periodic potential is altered [15]; for quantum heat transport through an ion chain, it is predicted that Fourier’s law is recovered when the ion spacing becomes constant [21].
- *Quantum communication* when coupling ions through fibers, for example, for a quantum internet [22–25], the strong coupling limit is difficult to reach and can be improved by cooperative effects [26, 27]. The cooperativity might be maximized by matching ion separation and the periodicity of the cavity mode. In general, the interaction of ions with standing waves can be optimized by matching the ion separation to periodicity of the standing wave. For larger strings, this can benefit from an equidistant spacing with applications in quantum information, quantum simulations or precision spectroscopy [28, 29].

This paper is part of the topical collection “Quantum Repeaters: From Components to Strategies” guest edited by Manfred Bayer, Christoph Becher and Peter van Loock.

✉ Michael Johanning
johanning@physik.uni-siegen.de

¹ Department Physik, Naturwissenschaftlich-Technische Fakultät, Universität Siegen, 57068 Siegen, Germany

- *Parallel precision spectroscopy* arrays of trapped ions are interesting for parallel precision spectroscopy and atomic clocks [30]. Such an array might be created either by a large number of individual microtraps or by a lower number of potentially anharmonic linear traps each holding a string of ions.
- Even though there is no fundamental limit for the size of harmonically trapped ions strings, practical limitation arises when adding more ions to an axially harmonic trapping potential. At a critical ion number, a transition from a linear to a zigzag configuration occurs [31–33]. The transition can be pushed toward higher ion numbers by a stronger radial confinement, but this approach is usually limited by technical constraints, such as flashovers due to high radio-frequency voltages. Weakening the axial confinement has the same effect but results in a very soft lowest mode and unfavorable trapping conditions.

Alterations of the harmonic trapping by a quartic component have been investigated to minimize the inhomogeneity of the density [10], and the influence of small anharmonicities on the axial normal modes is described in [34]. Instead of altering a harmonic potential to find more homogeneous ion arrangements, one might directly ask for the potential that yields the desired density distribution (with an anharmonicity that does not need to be handled in a perturbative manner), but analytic solutions exist for few special cases only. We follow an inverse approach where we ask for the electric field which is created by the desired ion distribution, here a string of equidistant ions, and then counterbalance that field at the locations of the ions. This approach can be used to calculate the voltages applied to segmented trap electrodes to obtain any desired position configuration, in principle only limited by the size and number of the trap segments. Alternatively, the electrode geometry might be optimized to yield the desired crystal configuration even with only two non-vanishing voltages.

Once the potential is found, one directly obtains a solid-state like band structure of normal modes and analytic energy values for the band edges. Since only the field needs to be compensated to keep the ions in the desired positions, the potential curvature at each ion is a free parameter and the normal mode spectrum can be varied; one possible particular modification is that the lower band edge can be kept at a finite value for any string length. Since the normal mode spectrum determines the effective spin–spin coupling between ions exposed to a magnetic gradient [35], the coupling pattern can be tailored in the same way. Anharmonic traps designed in such a way

allow to store linear strings of any length while the lowest and highest mode approach finite asymptotic values as expected for large periodic systems. This is an essential property for scalable quantum information processing and is in contrast to harmonic traps, where, for strings of growing size and constant radial confinement, the lowest transverse modes approach zero and thus the system undergoes a structural phase transition.

Also, leaving the regime of linear ion configurations might be interesting with anharmonic traps: The transition from a linear to a planar zigzag structure occurs at a specific radial trapping frequency for a given ion density [31, 32], as the Coulomb potential of all neighbor ions acts as a softening of the radial confinement. This softening becomes stronger for smaller ion distances. As the ion density in a harmonic trap peaks at the string center and increases with ion number [36], the transition to a zigzag is triggered there. Recent work on the Kibble–Zurek mechanism, which investigates the statistics of defect formation was carried out in linear ion traps [30, 37–39]. The trapping potentials discussed here allow to investigate finite size effects on the transition and defect formation statistics and thus the investigation of the transition from the homogeneous to the inhomogeneous Kibble–Zurek effect. The quantum nature of the transition to the zigzag has been investigated in [40, 41]. Anharmonic traps might thus be interesting for the creation of multiparticle entanglement near the zigzag transition and for the simulation of quantum critical phenomena typical for ferromagnetic systems.

The anharmonic axial confinement discussed here is not the only route to obtain homogeneous ion strings. Ion strings immersed into big ion crystals of different mass are also found to have a nearly perfect homogeneous spacing [42]. But in contrast to the approach presented here the surrounding crystal is subject to micromotion with possible detrimental effects, for instance, in terms of heating. Homogeneous crystals can also be created with periodic boundary conditions in ring traps [31].

This article is structured as follows: In Sect. 2, we construct a potential that results in a perfectly homogeneous spacing. Then, we calculate normal modes and discuss how to tune them without affecting the equilibrium positions in Sect. 3. We briefly investigate the transverse confinement and the transition to a zigzag for a homogeneous string in Sect. 4. The effective spin–spin coupling which arises when the ions are exposed to a magnetic gradient is analyzed in Sect. 5. Finally, we discuss the generation of a suitable potential in a segmented trap in Sect. 6, introducing a numerical method based on the Schmidt decomposition or in surface traps with optimized electrode shapes, before we conclude.

2 Electrostatic potentials for linear strings of equidistant ions

We start with a string of N equally spaced ions with separation d centered around the origin, extending from $-\bar{z}_{\max}$ to \bar{z}_{\max} . The length of the chain is thus $(N - 1)d = 2\bar{z}_{\max}$, and the equilibrium position of the i th ion is

$$\bar{z}_i = -\frac{N - 1}{2}d + (i - 1)d. \tag{1}$$

The i th ion will have n_l left neighbors ions and n_r right neighbors ions with

$$n_l(i) = i - 1 \quad \text{and} \quad n_r(i) = N - i \tag{2}$$

and the separation of ions i and j is $d_{ij} = d(i - j)$ with positive values of d_{ij} indicating that ion j sits left of ion i . The field seen by ion i is the sum of the fields of all neighbors, thus

$$\begin{aligned} E_N(i) &= \frac{q}{4\pi\epsilon_0} \frac{1}{d^2} \left(\sum_{n=1}^{n_l} \frac{1}{n^2} - \sum_{n=1}^{n_r} \frac{1}{n^2} \right) \\ &= E_{\text{nn}} \left(H_{n_l}^{(2)} - H_{n_r}^{(2)} \right), \end{aligned} \tag{3}$$

with E_{nn} being the electric field strength created by the next neighbor given by

$$E_{\text{nn}} = \frac{q}{4\pi\epsilon_0} \frac{1}{d^2} \tag{4}$$

and $H_n^{(m)}$ being the generalized harmonic number of order m given by

$$H_n^{(m)} = \sum_{k=1}^n \frac{1}{k^m}. \tag{5}$$

Since all separations are identical, forces can cancel pairwise, up to the excess ions. Without any loss of generality, we assume $n_l > n_r$ and obtain

$$\begin{aligned} E_N(i) &= E_{\text{nn}} \sum_{n=n_r+1}^{n_l} \frac{1}{n^2} \\ &= E_{\text{nn}} \left[\psi^{(1)}(n_r + 1) - \psi^{(1)}(n_l + 1) \right], \end{aligned} \tag{6}$$

using the trigamma function $\psi^{(1)}(x)$ which is a representative of the polygamma functions $\psi^{(m)}(x)$ (see Appendix 1).

A potential $\phi_N(z)$ which compensates all Coulomb repulsions would need to yield the electric field fulfilling

$$-\frac{d}{dz} \phi_N \Big|_{z=\bar{z}_i} = -E_N(i) \tag{7}$$

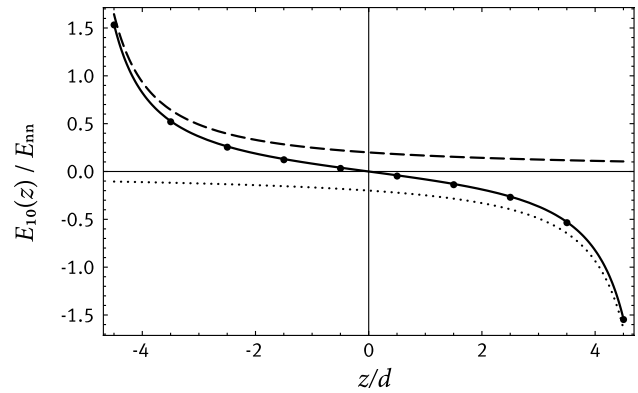


Fig. 1 The electrostatic field $E_{10}(z)$ which compensates the Coulomb repulsion of a string of 10 ions, centered at the origin with next-neighbor separation d . The solid line depicts the electric field, and the dashed and dotted traces show the constituting trigamma functions $\psi^{(1)}(N_+ + z/d)$ and $\psi^{(1)}(N_+ - z/d)$, respectively. Ions are marked as dots, indicating their position and the field strength they experience by the external potential. Positive values of the electric field refer to a force pushing the ion to the right

This requirement only needs to be fulfilled at all ion positions, but not in between. This gives considerable freedom in designing a trapping potential, which will be explored later. One boundary condition certainly remains: The total energy needs to be minimized with the ions placed at the positions \bar{z}_i . The solution for the field distribution in terms of the trigamma function suggests a continuous interpolation between ions due to the continuous character of ψ . To give a spatial representation of the potential, we can identify the continuous counterparts \tilde{n}_l and \tilde{n}_r to our discrete definition in Eq. (2) as

$$\tilde{n}_l(z) = \frac{N - 1}{2} + \frac{z}{d} \quad \text{and} \quad \tilde{n}_r(z) = \frac{N - 1}{2} - \frac{z}{d} \tag{8}$$

with $\tilde{n}_l(\bar{z}_i) = n_l(i)$ and $\tilde{n}_r(\bar{z}_i) = n_r(i)$. Using $N_+ = (N + 1)/2$ and the dimensionless $\tilde{z}_{\pm} = N_+ \pm z/d$ the electric field which will compensate all repulsions takes the form

$$E_{\phi_N}(z) = E_{\text{nn}} \left[\psi^{(1)}(\tilde{z}_+) - \psi^{(1)}(\tilde{z}_-) \right] \tag{9}$$

An example for $N = 10$ ions is shown in Fig. 1. Finally, the potential with some arbitrary offset $\phi_0 = \phi_N(z = 0)$ yields

$$\phi_N(z) = \phi_0 - \int_0^z E_{\phi_N}(\xi) d\xi \tag{10}$$

and thus

$$\phi_N(z) = \phi_{N,0} - E_{\text{nn}}d \left[\psi^{(0)}(\tilde{z}_+) + \psi^{(0)}(\tilde{z}_-) \right], \tag{11}$$

with the choice

$$\phi_{N,0} = 2E_{\text{nn}}d \psi^{(0)}(N_+) \tag{12}$$

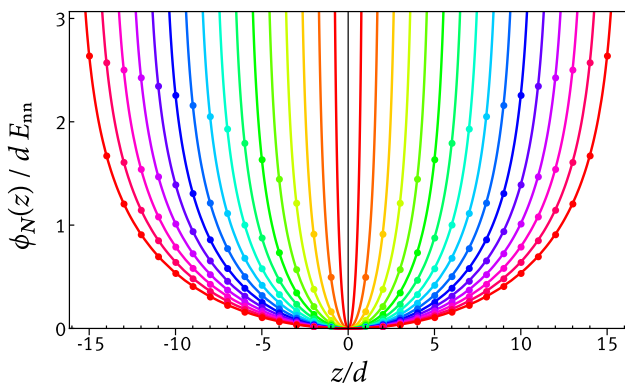


Fig. 2 Electrostatic potentials to generate equally spaced strings of an uneven number of ions from 1 (orange) to 31 (red) ions and next-neighbor separation d . The notion of constant spacing starts to be meaningful for symmetric potentials and string lengths above three; the formal potential solutions for smaller N exist and are included for completeness. The ion positions with their energy in the external potential are indicated by the dots

yielding $\phi_N(0) = 0$. Potentials and equilibrium positions for uneven $N = 1, \dots, 31$ ions and a constant spacing d are shown in Fig. 2.

The Taylor series of the potential around the origin has only even contributions and is given by

$$\phi_N(z) = -E_{nn}d \sum_{n=1}^{\infty} \frac{2\psi^{(2n)}(N_+)}{(2n)!} \left(\frac{z}{d}\right)^{2n}. \quad (13)$$

The coefficients depend on the desired ion number and spacing. From the coefficients, it becomes clear that this potential is not a generalization of [10] where a quartic term was optimized for a specific ion number to minimize distance variations. In contrast to [10], the quadratic and quartic term (as well as all others) found here have positive coefficients.

For large ion numbers N and low order n , the Taylor coefficients can be approximated as

$$\lim_{N \rightarrow \infty} \psi^{(2n)}(N_+) = -\frac{(2n)!}{2nN_+^{2n}}. \quad (14)$$

The potential further simplifies to (using $N_+ \approx N/2$)

$$\phi_N(z) \approx E_{nn}d \sum_{n=1}^{n_{\max}} \frac{1}{n} \left(\frac{2z}{Nd}\right)^{2n} \quad (15)$$

when not too high orders contribute, which is well fulfilled in the central region of the string. Here, the potential remains constant if z/N is kept fixed and we obtain

$$\phi_{\alpha N}(\alpha z) \approx \phi_N(z) \quad (16)$$

This is shown in Fig. 3, and a potential with the ratio of the Taylor coefficients, as given by Eq. (15), will trap strings

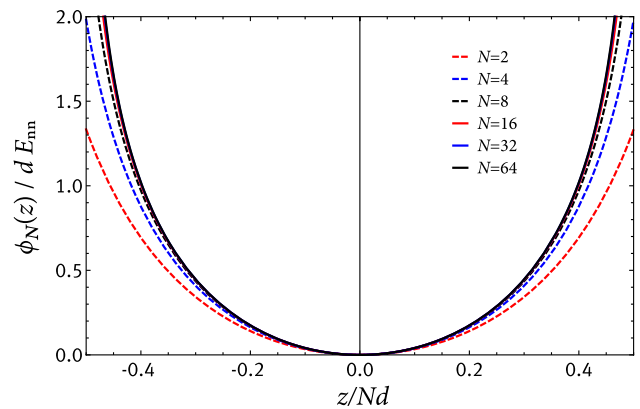


Fig. 3 Anharmonic potential according to Eq. (11) as a function of z/Nd . For $N > 16$ the traces become almost indistinguishable

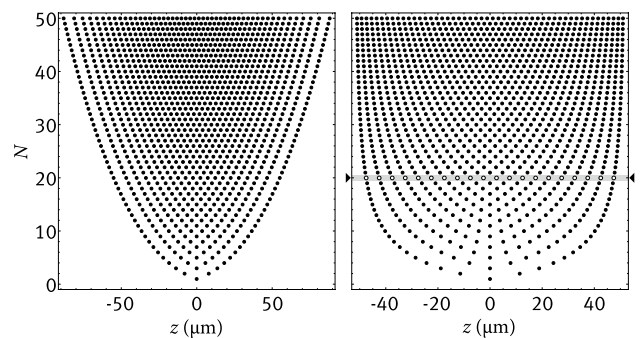


Fig. 4 Numerically obtained equilibrium positions of ions loaded into a harmonic potential (left) and an anharmonic potential according to Eq. (11) (right) for strings of length N (vertical axis): The simulations were carried out for $^{172}\text{Yb}^+$ and a trap frequency of $\omega_z = 2\pi \times 100$ kHz for the harmonic trap. The anharmonic trapping potential was optimized to yield a homogeneous spacing of $d = 5 \mu\text{m}$ for $N = 20$ ions (marked in gray and with arrows). The most obvious features of the ion strings in the anharmonic potential are the absence of increased ion spacings toward the string's ends and the almost constant string length for large ion numbers

of varying ion number with approximately constant spacing throughout the string, where the spacing is approximately inverse proportional to the ion number.

Ion distributions for a constant harmonic potential and for a constant anharmonic potential are compared in Fig. 4 for various ion string lengths. The inhomogeneity of the ion density is compared to that of a harmonic trap in Fig. 5 for varying ion numbers: The anharmonic trapping outperforms harmonic trapping (in terms of homogeneity) for the chosen parameters and $N > 12$ typically by a factor larger than five.

A noticeable difference compared with harmonic trapping is the effect of homogeneous stray fields: For a strictly harmonic trap, this only shifts the center of mass position of the ion crystal but leaves the ion separations invariant.

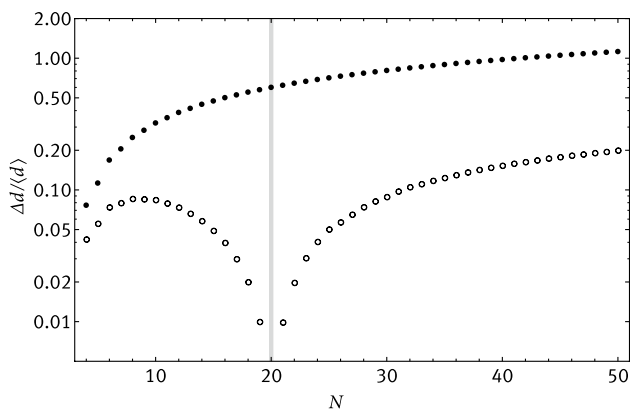


Fig. 5 Inhomogeneities of the ion separation for harmonically (*dots*) and anharmonically (*open circles*) trapped ions. The anharmonicity was chosen to give constant spacing for $N = 20$ ions. The inhomogeneity is expressed as the difference of the largest and smallest separation $\Delta d = d_{\max} - d_{\min}$ normalized to the average separation $\langle d \rangle$. As expected, the inhomogeneity of the ion spacing vanishes for the designed ion number. For this anharmonic potential and ion numbers $N > 12$ the variation of the ion separation it is at least a factor of five lower compared to harmonic trapping

For anharmonic trapping, a homogeneous stray field also breaks the constant spacing; but when compensating the stray field by nulling the displacement of a single ion in that trapping potential by position sensing as described in [43], the relative inhomogeneities can be reduced to a per mille level.

It should be noted that the polygamma functions $\psi^{(n)}(x)$ exhibit singularities for all $-x \in \mathbb{N}_0$, and thus, the electric fields and potentials have a singularity for the smallest $|z|$ at the positions $|z/d| = N_+$. The compensation of fields holds only in the range $z/d \in [-N_+ + 1; N_+ - 1]$. There are no singularities inside the crystal, but the proximity to the singularities requires increasing potential curvatures. The curvature of the potential is given by

$$\phi_N''(z) = -\frac{E_{nn}}{d} \left[\psi^{(2)}(\bar{z}_+) + \psi^{(2)}(\bar{z}_-) \right] \tag{17}$$

At the positions of the ions \bar{z}_i , this evaluates to

$$\phi_N''(\bar{z}_i) = -\frac{E_{nn}}{d} \left[\psi^{(2)}(i) + \psi^{(2)}(N + 1 - i) \right]. \tag{18}$$

Using

$$\psi^{(2)}(n) = 2H_{n-1}^{(3)} - 2\zeta(3) \tag{19}$$

for $n \geq 1$ [44], where $\zeta(x)$ refers to the Riemann zeta function, we obtain

$$\phi_N''(\bar{z}_i) = \frac{E_{nn}}{d} \left(4\zeta(3) - 2H_{i-1}^{(3)} - 2H_{N-i}^{(3)} \right). \tag{20}$$

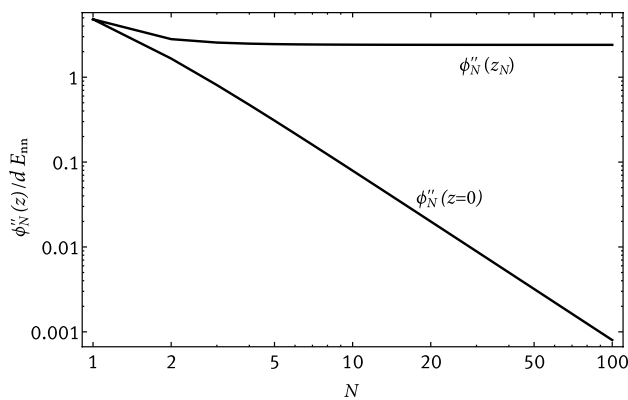


Fig. 6 Potential curvature at the position of the outermost ion (where it is largest) and at the *center* of the potential (where it becomes minimal). The maximum curvature is independent of the ion number for large ion strings

As shown in Fig. 6, the potential curvature seen by the outer ion approaches an asymptotic limit for large N , whereas the curvature at the trap center approaches zero as N^{-2} and the center of mass mode becomes increasingly soft; a way to avoid this is discussed in the next section.

Another concern could be that the anharmonicity might be too large, so that the normal mode ansatz (discussed in detail in the following section) might not be justified anymore. To quantify this, we compare the third derivative of the trapping potential at the position of the outermost ions, where it is largest,

$$\phi_N'''(\bar{z}_{\max}) = \frac{E_{nn}}{d^2} \left[\psi^{(3)}(1) - \psi^{(3)}(N) \right] \tag{21}$$

to the anharmonicity of the Coulomb potential, which, at distance d , becomes

$$\phi_C'''(d) = 6 \frac{E_{nn}}{d^2}. \tag{22}$$

The ratio $\phi_N'''(\bar{z}_{\max})/\phi_C'''(d)$ is almost independent of the ion number and approaches $\pi^4/90 \approx 1.08232$ for large ion numbers. Thus, it is of almost identical size compared with the Coulomb anharmonicity unavoidably present and usually not considered critical in the discussion of normal modes of cold ion strings.

3 Axial dynamics

The normal modes of an ion crystal are obtained by approximating the total energy up to second order in ion displacements from their respective equilibrium position, refer to Appendix 2 for the detailed ansatz and the notation used in the following. The resulting system of equations

can then be solved for eigenstates and their corresponding eigenfrequencies.

3.1 Axial normal modes

The axial normal mode matrix \hat{K} for an ion crystal is given as

$$K_{ij} = \left. \partial_{z_i} \partial_{z_j} E_{\text{tot}} \right|_{z_i=\bar{z}_i, z_j=\bar{z}_j} = \left. \partial_{\delta_i} \partial_{\delta_j} E_{\text{tot}} \right|_{\delta_i=\delta_j=0} \quad (23)$$

with the total potential energy E_{tot} (including the external potential and mutual Coulomb repulsion) and the excursions δ_i from the equilibrium positions \bar{z}_i . For the off-diagonal elements, this evaluates to

$$K_{i \neq j} = -\frac{q^2}{4\pi\epsilon_0} \frac{2}{|\bar{z}_i - \bar{z}_j|^3} = -\frac{qE_{\text{nn}}}{d} \frac{2}{|i-j|^3} \quad (24)$$

which is independent of the trapping potential (it depends implicitly on the potential, as it depends on equilibrium positions), whereas for the diagonal elements we obtain

$$K_{ii} = q\phi''(\bar{z}_i) - \sum_{j \neq i} K_{ij} \quad (25)$$

By shifting the summation bounds, this can again be related to harmonic numbers [see Eq. (5)],

$$K_{ii} = q\phi''(\bar{z}_i) + \frac{2qE_{\text{nn}}}{d} \left(\sum_{j=1}^{i-1} \frac{1}{j^3} + \sum_{j=1}^{N-i} \frac{1}{j^3} \right) \quad (26)$$

$$= q\phi''(\bar{z}_i) + \frac{qE_{\text{nn}}}{d} \left(2H_{i-1}^{(3)} + 2H_{N-i}^{(3)} \right). \quad (27)$$

Using the second derivative of the potential as given in Eq. (20), the harmonic numbers cancel and we finally obtain

$$K_{ii} = 4\zeta(3) \frac{qE_{\text{nn}}}{d} \quad (28)$$

Equation (28) states not only that the ion spacing is constant, but also that the restoring force on each ion, which is a combined effect of the anharmonic trapping potential and the Coulomb potential of all other ions in the chain, is equal for all ions.

The matrix \hat{K} might be decomposed as

$$\hat{K} = \frac{qE_{\text{nn}}}{d} \left(4\zeta(3)\hat{1} + \hat{K}_N^{(r)} \right) \quad (29)$$

with $4\zeta(3)\hat{1}$ being the irrational and $\hat{K}_N^{(r)}$ being the rational part of the normal mode matrix (up to the prefactor qE_{nn}/d). Due to the structure of the eigenvalue problem [see Appendix 2, Eq. (56)], the eigenvalues κ_n of \hat{K} are the eigenvalues of the rational part $qE_{\text{nn}}/d \hat{K}_N^{(r)}$ shifted by

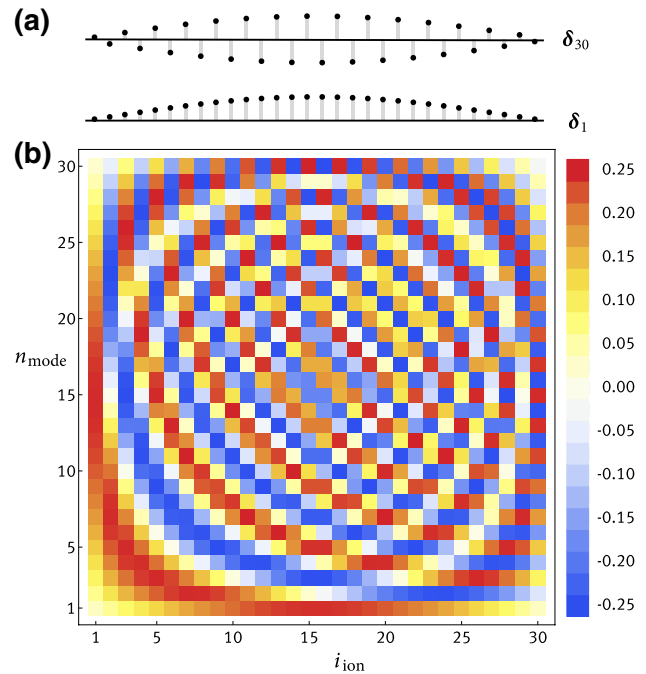


Fig. 7 Motional eigenstates of a chain of $N = 30$ ions. **a** Lowest eigenstate δ_1 and highest eigenstate δ_{30} : Both states have a sinusoidal envelope. The highest eigenstate differs from the lowest by an alternating excursion of neighboring ions. Excursions have been plotted in the transverse direction for visual clarity; **b** color plot of all motional eigenstates. Each mode is represented by one row, and each column represents one ion. Excursions of the normalized eigenstates are color-coded (compare color legend on the right side). The arbitrary phase of each eigenstate was chosen such that the excursion of the first ion is positive. The modes resemble the vibrational modes of a string

$4\zeta(3)qE_{\text{nn}}/d$. The eigenvalues of $\hat{K}_N^{(r)}$ are in general not rational, being the roots of the characteristic polynomial.

For example, the rational part of the normal mode matrix of six equidistant ions trapped in the potential given by Eq. (11) has the very regular form of a symmetric Toeplitz matrix (which means that K_{ij} depends only on the index difference $i - j$ [45])

$$\hat{K}_6^{(r)} = -2 \begin{pmatrix} 0 & 1 & \frac{1}{8} & \frac{1}{27} & \frac{1}{64} & \frac{1}{125} \\ 1 & 0 & 1 & \frac{1}{8} & \frac{1}{27} & \frac{1}{64} \\ \frac{1}{8} & 1 & 0 & 1 & \frac{1}{8} & \frac{1}{27} \\ \frac{1}{27} & \frac{1}{8} & 1 & 0 & 1 & \frac{1}{8} \\ \frac{1}{64} & \frac{1}{27} & \frac{1}{8} & 1 & 0 & 1 \\ \frac{1}{125} & \frac{1}{64} & \frac{1}{27} & \frac{1}{8} & 1 & 0 \end{pmatrix}. \quad (30)$$

Figure 7 shows motional eigenstates of the ion string in the anharmonic potential. The modes resemble the vibrational modes of a continuous string which seems plausible, as the potential, and its derivatives are singular at \bar{z}_0 and \bar{z}_{N+1} , and thus, the ion string can be thought of as being fixed there. As can be guessed from Fig. 7a), the excursion

of ion i in the lowest eigenstate $\delta_{1,i}$ (not normalized) resembles the pattern

$$\delta_{1,i} \approx \sin\left(\frac{i\pi}{N+1}\right).$$

This allows to calculate its eigenvalue which approaches zero for growing string length, correspondingly does the lowest mode, roughly inverse proportionally with N . The highest eigenstate (again, not normalized) resembles (compare Fig. 7a)

$$\delta_{N,i} \approx (-1)^i \sin\left(\frac{i\pi}{N+1}\right)$$

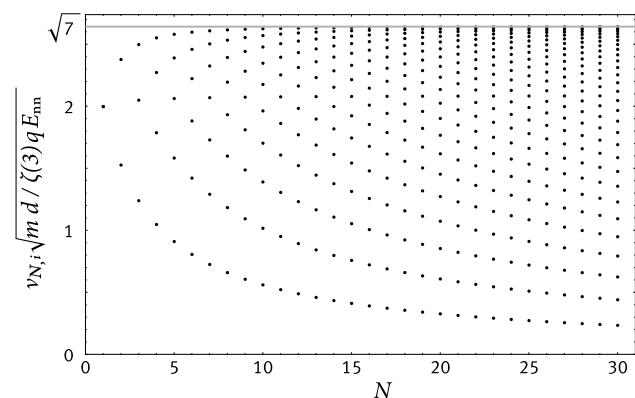


Fig. 8 Axial normal mode frequencies of an equidistant ion string. The eigenfrequencies are displayed as dots as a function of the ion number N . The asymptotic maximum eigenfrequency is plotted as a gray line. The eigenfrequencies fill a band which approaches a constant width for large N . The mode density peaks at the upper band edge. The frequency of lowest mode is roughly inversely proportional to the string length

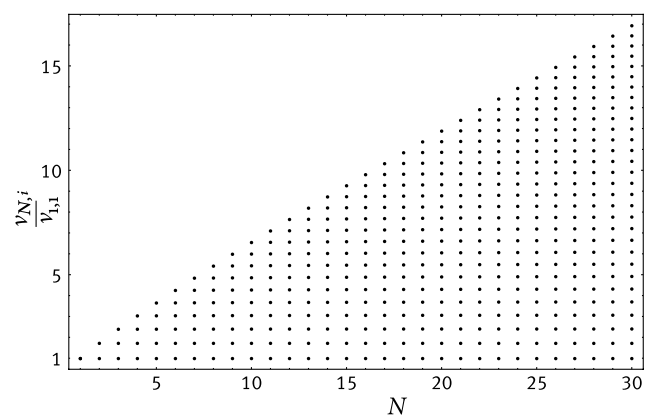


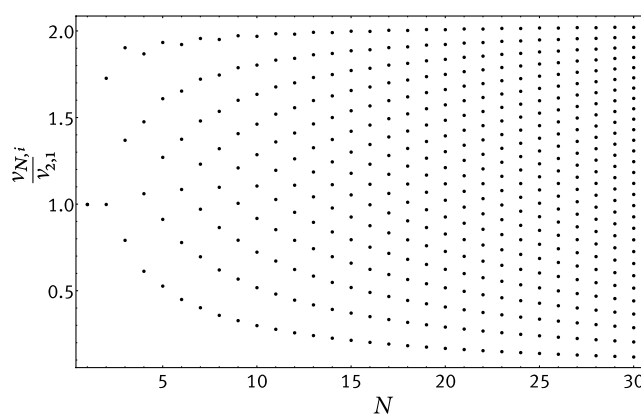
Fig. 9 Left Axial eigenmodes $v_{N,i}$ of up to $N = 30$ ions in a harmonic trap in units of the center of mass mode $v_{1,1}$. Modes of similar character (such as center of mass and breathing) have a frequency which is independent of ion number. The frequency of the highest mode grows approximately linearly with respect to ion number. Right the

and with this, the limit of highest eigenvalue computes to

$$\kappa_{\max} = \lim_{N \rightarrow \infty} \kappa_N = 7\zeta(3) \frac{qE_{nn}}{d}. \tag{31}$$

Figure 8 shows the eigenfrequencies of the matrices \hat{K}_N for ions with a mass m . For increasing string length, the eigenvalues fill a band which approaches a constant width of κ_{\max} for large N , as it would be expected for an extended solid-state system. The vanishing energy of the lower band edge, or of the mode structure altogether, can be altered by mode tuning as detailed in Sect. 3.2, making this system potentially interesting for quantum simulations of solid-state systems.

It is instructive to compare this to harmonically trapped ion strings of growing length: If the trapping potential is kept constant, modes of similar character have a constant frequency independent of chain length N (compare Fig. 9, left) and the frequency of the highest mode grows without limit. At some point, the highest mode even exceeds the trap drive frequency, possibly making the system more susceptible to near resonant heating by the drive. If, on the other hand, the maximum ion density is kept constant, the lowest mode is more and more softened, the mode density grows and the modes also fill a band (compare Fig. 9, right). As the band of modes has a width independent of ion number for a given ion separation, the mode density increases inversely to the ion number. The pattern in which ions participate in modes is also qualitatively different for harmonic trapping: whereas for the center of mass modes all ions contribute equally, with increasing mode energy only a shrinking core in the center of the string participates in the oscillation (see Fig. 10).



same modes for a harmonic trap, but the trap was softened for $N > 2$ ions to keep the minimum separation near the trap center constantly equal to the ion separation for a string of two ions. The mode density is almost constant, and the frequency of the lowest mode is roughly inversely proportional to the string length

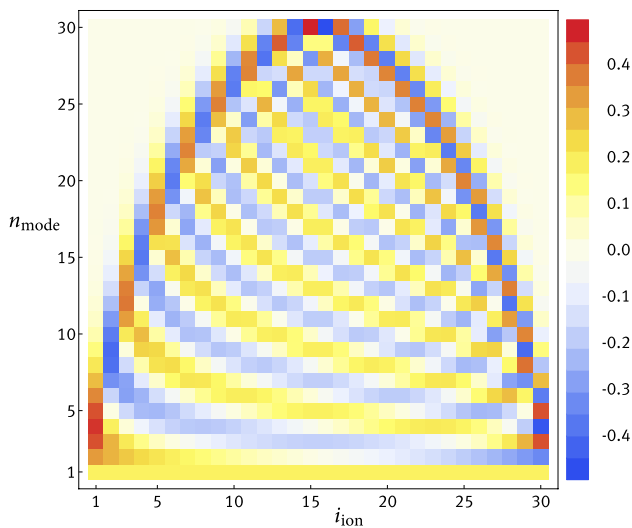


Fig. 10 Eigenstates of 30 ions in a harmonic trap. The representation is identical to Fig. 7. For the center of mass mode, all ions oscillate with uniform amplitude. With increasing mode frequency, fewer and fewer ions participate in the mode, building a bulk of shrinking size, where the ions close to the outer edges of the bulk oscillate the strongest

3.2 Tuning of axial modes

The eigenvalue problem of the normal mode matrix suggests a simple way for the alteration of the eigenvalues: If the matrix \hat{K} has eigenvalues κ_n , then the matrix $\hat{K}' = \hat{K} + \kappa_0 \hat{1}$ has the eigenvalues $\kappa_n + \kappa_0$ and its eigenvectors δ_n remain the same, as

$$\begin{aligned} \hat{K}' \delta_n &= (\hat{K} + \kappa_0 \hat{1}) \delta_n = (\hat{K} + m v_0^2 \hat{1}) \delta_n \\ &= m (v_n^2 + v_0^2) \delta_n = m v_n'^2 \delta_n \end{aligned} \tag{32}$$

This means that adding a constant curvature $m v_0^2 / 2$ to the anharmonic potential would raise all modes from v_n to $\sqrt{v_n^2 + v_0^2}$ if the ion positions would remain unaffected. For isospaced ions, a natural solution to obtain an additional curvature but no additional force at equidistant points is the addition of the dipole potential of a standing wave generated by crossed laser beams of identical wavelength: The periodicity of the standing wave is given by the wavelength used and the intersection angle and can be made an integer fraction of the ion separation. If the extrema of the standing wave are placed at the ion positions, the curvature seen by each ion can be changed without displacing the ion.

The additional curvature from such a standing wave leaves the differences between eigenvalues invariant and does not change the eigenstates. But even this simple alteration may be useful to shift all eigenvalues to positive values and thus to restore stability. Adding a multiple of

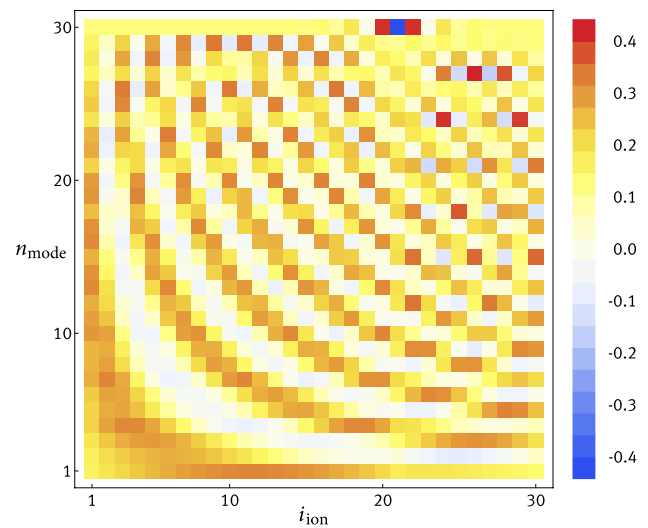


Fig. 11 Eigenstates for a string of equidistant ions with additional mode shaping. The representation follows Fig 7. An additional axial confinement for ion $i_d = 21$ creates a local defect and drastically alters the symmetry of the motional eigenstates of the entire crystal. The energy of the modes, however, remains largely unaffected

an identity matrix to the mode matrix can make the mode matrix approximately diagonal, if the multiplier is much bigger than all other entries, and thus, the system becomes almost non-interacting or on the other hand more strongly interacting, if the eigenvalues are lowered.

By adding a standing wave with a modulated spatial envelope, one can affect the band structure and the coupling pattern. Superimposing different standing waves from lasers pairs with different relative phases, detunings or polarizations allows to construct a variety of coupling matrices. The power of mode tuning as sketched above is illustrated by two examples:

1. Modifying the potential curvature for only one ion i_d by changing a single diagonal element of the normal mode matrix

$$K'_{ii} = K_{ii} + m v_d^2 \delta_{i,i_d} \tag{33}$$

corresponds to a lattice defect of variable strength given by v_d . The symmetry of the motional eigenstates can be dramatically altered, and one localized eigenstate can be isolated where almost only the defect ion is contributing to the mode (see Fig. 11).

2. Adding a periodic pattern with a period larger than the ion separation corresponds to a superlattice that can split the band of motional states into sub-bands or even single out modes, such that they can be isolated from all bands and individually addressed even for large samples (see Fig. 12).

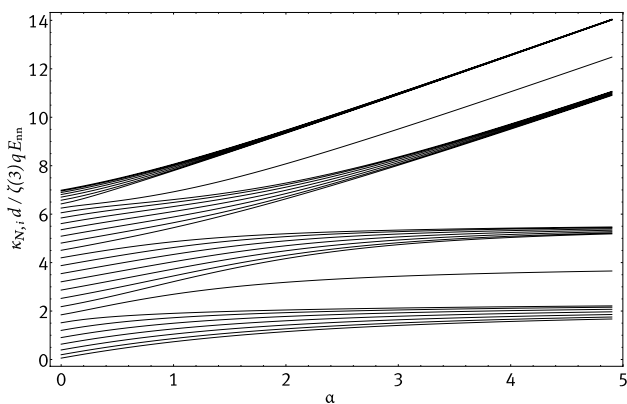


Fig. 12 Eigenvalues of an equidistant string of $N = 30$ ions subject to an additional periodic potential of varying strength α . The additional potential splits the motional bands and may isolate single modes, such that they may be addressed easily, even in very large samples

For a noticeable effect, the curvature of the dipole potential needs to have a size comparable to the diagonal elements of the unmodified normal mode matrix. To compare the two curvatures, we start with a light shift ΔE_{dip} spatially modulated with a sinusoidal envelope. If the detuning δ is large compared to the hyperfine structure, the light shift simplifies to $\Delta E_{\text{dip}} = -\hbar\Omega^2/4\delta$ and the optical potential is given by

$$\Delta E(z) = -\hbar \frac{\Omega^2}{\delta} \sin\left(\frac{\pi}{d'}z\right)^2 \tag{34}$$

with Rabi frequency Ω , as the period d' is required to be a fractional of the ion separation $d' = d/n, n \in \mathbb{N}$. The maximum curvature of this potential is then

$$\partial_z^2 \Delta E(z) \Big|_{z=0} = -\frac{2\hbar\Omega^2}{\delta} \frac{n^2\pi^2}{d^2}. \tag{35}$$

Making this curvature equal to the unmodified curvature K_{ii} requires a Rabi frequency of

$$\Omega = \sqrt{\frac{\zeta(3)}{2n^2\pi^3} \frac{q^2}{\hbar\epsilon_0 d}} \delta \tag{36}$$

(which is independent of ion mass), or equivalently an intensity

$$I = \frac{2\Omega^2}{\Gamma^2} I_s = \zeta(3) \frac{q^2}{\pi^3 \epsilon_0 n^2 d} \frac{\delta}{\hbar \Gamma^2} I_s \tag{37}$$

K_{ii} corresponds to an oscillation frequency between 2 and 9 kHz for ions with masses between those of Beryllium and Ytterbium and for an ion separation of 5 μm . Much larger trapping frequencies have been observed in traveling and standing wave dipole traps [46, 47].

4 Transverse confinement and the transition to a planar zigzag configuration

While increasing the number of trapped ions in a harmonic trap, the central ion density increases and at critical ion densities transitions to a planar zigzag and later to three-dimensional structures occur [48, 49]. Correspondingly, the transition to a zigzag can be induced for a fixed ion number by a softening of the radial confinement. For degenerate radial trap frequencies, this critical point is given, when the radial anti-binding curvature is exactly compensated by the rf effective potential with trap frequency ω_r . Using Eq. (28) yields

$$\omega_r^{\text{crit}} = \sqrt{\frac{\kappa_{\text{max}}}{2m}}, \tag{38}$$

with the ion mass m and using κ_{max} from Eq.(31). Besides being a practical limitation for the size of linear ion strings, the transition can certainly be viewed as a feature, as it allows to create 2d and 3d structures already in linear ion traps with rich physics at and beyond the critical point [30, 33, 37–39, 50].

4.1 Three-dimensional potential

A rotationally symmetric potential fulfilling Laplace’s equation in the vicinity of the z -axis ($r \ll Nd$) has the approximate shape

$$\phi(r, z) \approx \phi(z) - \frac{1}{4}\phi''(z) r^2 \tag{39}$$

Strictly speaking, fulfilling Laplace’s equation requires an anharmonicity in the radial direction, which compensates the anharmonicity in the axial direction. We focus here on crystals with small radial extent to keep the effect of excess micromotion small. For linear strings and for the transition from a string to a long, narrow zigzag, the radial coordinates remain much smaller compared with the axial, and the radial anharmonicity is neglected. Using Eqs. (11), (12), (17) and (39), we obtain

$$\begin{aligned} \frac{\phi_{3d}(r, z)}{E_{\text{nd}}} &\approx 2\psi^{(0)}(N_+) - \psi^{(0)}(\tilde{z}_+) - \psi^{(0)}(\tilde{z}_-) \\ &+ \left[\psi^{(2)}(\tilde{z}_+) + \psi^{(2)}(\tilde{z}_-) \right] \frac{r^2}{4d^2} \end{aligned} \tag{40}$$

In experimental realizations, a lifting of the degeneracy of the radial trap frequencies might be desirable, but Eq. (40) can serve as a starting guess. A potential as given in Eq. (40), and with a superimposed radial confinement from the effective rf potential, is shown in Fig. 13.

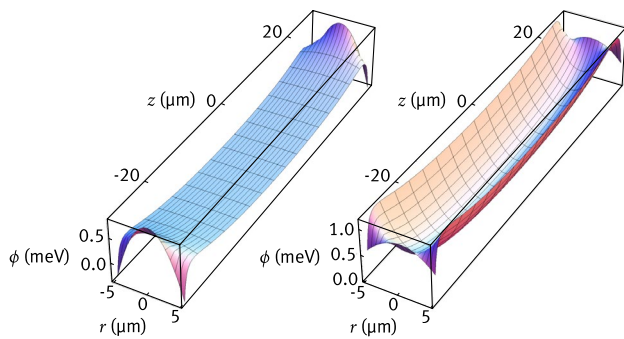


Fig. 13 Radial and axial confinement in an anharmonic trap. *Left* dc potential which satisfies Laplace's equation and results in an axially oriented linear string of 11 Yb ions with an equal separation of 5 μm . The potential is necessarily radially anti-binding. *Right* an additional *rf* effective potential with a radial trap frequency of 1 MHz is sufficient to stabilize the crystal radially

4.2 Transverse modes

With the knowledge of the potential distribution and the ion positions, the three-dimensional normal mode matrix can be calculated. As discussed for harmonic traps in [20, 36], the mode matrix can be expressed as a $3N \times 3N$ -matrix. It becomes block diagonal for a linear ion string, and the coupling of radial and axial modes vanishes. For a linear crystal of equidistant ions, the radial part becomes

$$\hat{K}_{x,y} = -\frac{1}{2}\hat{K}_z + m\omega_{x,y}^2 \hat{1} \quad (41)$$

where \hat{K}_z is given by Eq. (29). The radial mode matrices are Toeplitz as well and the radial eigenvalues are identical to the axial ones, up to a prefactor of $-1/2$ and a shift of $m\omega_{x,y}^2$. As a consequence, also the radial eigenvalues form a band with a width that is independent of the radial confinement and approaches the asymptotic value $\kappa_{\text{max}}/2$ [see Eq. (31)] for large N . The width of the band in frequency space, however, is not constant and can be very narrow for strong radial confinement, as shown in Fig. 14.

The radial and axial modes form well-separated bands for tight radial confinement. As the radial confinement is softened, the bands start to overlap, until the lowest radial mode approaches zero and the crystal rearranges to a zigzag. The dependence of the overlap of radial and axial modes on the radial confinement is shown in Fig. 15. As discussed in Sect. 3.2, the additional radial *rf* confinement gives much simpler access to the global tuning of the diagonal elements of the transverse mode matrix compared to a tuning of axial modes.

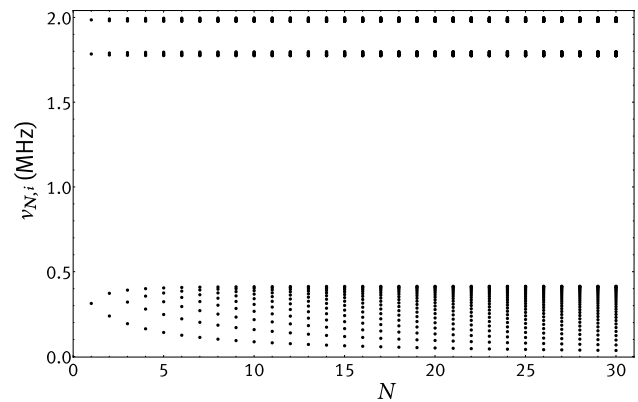


Fig. 14 Isospaced axial and radial modes for linear crystals of Yb ions for varying length N , with an axial separation $d = 10 \mu\text{m}$, and a transverse confinement $\omega_x = 2\pi \times 2 \text{ MHz}$, $\omega_y = 2\pi \times 1.8 \text{ MHz}$. For these parameters, the modes form three well-separated bands (from lower to higher frequency along z , y and x). The widths of the transverse mode bands are 22 and 24 kHz, respectively

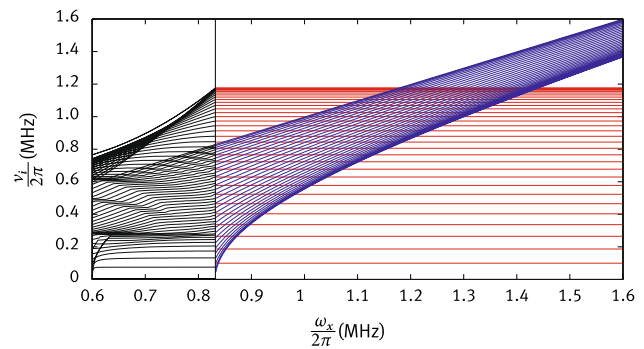


Fig. 15 Modes of a crystal of equidistant $^{171}\text{Yb}^+$ -ions with a spacing of 5 μm , subject to variable transverse confinement in the x -direction. For large transverse confinement, the radial modes (*blue*) form a narrow band above the axial modes (*red*). As the transverse confinement is lowered, the axial and radial modes overlap and at some point the lowest radial mode approaches zero. Below this critical radial confinement (indicated by a *vertical line*), the ion crystal rearranges to a zigzag, and none of the modes has a pure axial or radial character

4.3 Transition to a planar zigzag configuration

In a harmonic trap, the lateral extension of a zigzag crystal peaks at the center of the ion crystal, as the axial ion density is maximum here. One expects, from the constant axial ion density of the strings described in this article, a homogeneous lateral extension, when ions in such an anharmonic trap undergo the transition to the zigzag.

With a potential as given in Eq. (40), we numerically calculated equilibrium positions of ion strings in 2-d (assuming a stronger radial confinement along the third

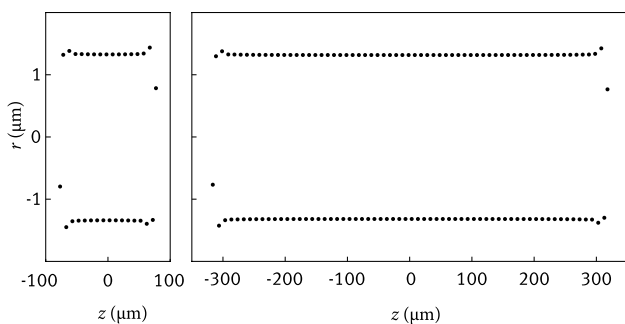


Fig. 16 Two-dimensional ion crystals of 32 (*left*) and 128 (*right*) ions. Note the different scaling for the *horizontal* and *vertical* axis. Both configurations were calculated for $^{171}\text{Yb}^+$, an axial separation of 5 μm and a radial trap frequency of $\omega_{\text{rad}}/2\pi = 700$ kHz. Effects of finite chain size are of identical extent and magnitude for the two cases despite different crystal size and affect approximately only the outermost 5 ions at either end

direction to fix the principal axes), and two examples are displayed in Fig. 16. A striking feature is the almost perfect homogeneous width of the zigzag. Only a small number of ions, independent of the size of the chain, deviates from the regular pattern at either end.

From the calculation of the diagonal elements of the normal mode matrix, we saw that the axial curvature seen by each ion is identical for all ions. As the electrostatic potential needs to fulfill Laplace’s equation, also the anti-binding radial effect of this potential must be of equal strength at each ion position, and one could expect a zigzag formation more closely resembling the condition of an infinitely extended string or periodic boundary conditions, as created in ring traps [31, 32]. Repeating the calculation for strings of various lengths, we varied the radial confinement and analyzed the lateral extension of the crystal, as a function of radial confinement, as shown in Fig. 17. Fitting a power law for the standard deviation of the transverse ion positions σ_x , we can obtain the transition frequency as a function of crystal size. Finite size effects always give a transition frequency below ω_r^{crit} [see Eq. (38)]. Good agreement is obtained already at medium crystal sizes (sub-percent for $N > 8$), and the deviation from the asymptotic value approximately vanishes as N^{-2} .

5 Spin–spin coupling in a constant magnetic gradient

When the states of the ions used for a quantum register are chosen to be magnetic field sensitive hyperfine levels of the electronic ground state, an inhomogeneity of the magnetic field along the string lifts the degeneracy of qubit splittings and the ions can be addressed in frequency space [5, 51–53]. Very low crosstalk can be achieved even at moderate

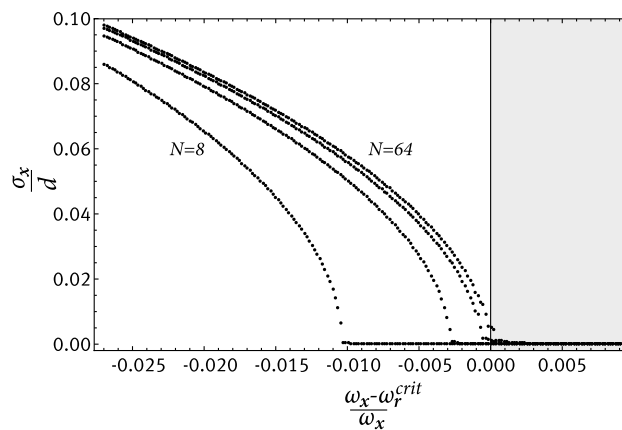


Fig. 17 Lateral crystal size from numerical simulations as a function of radial confinement ω_x and ion number N . The standard deviation of the transverse ion positions in units of the axial ion separation is plotted against the relative deviation from the predicted transition frequency ω_r^{crit} [see Eq. (38)]. The ion number rises in powers of two from 8 (*leftmost curve*) to 64 (*rightmost curve*). Simulations were carried out for $^{171}\text{Yb}^+$ and an axial separation of 5 μm , yielding the transition frequency $\omega_r^{\text{crit}} \approx 2\pi \times 832.4$ kHz. Fitting a power law for the standard deviation below the transition shows that the deviation from the asymptotic transition frequency vanishes proportional to N^{-2}

magnetic field gradients [7]. For homogeneous magnetic field gradients and ion separations, the single qubit resonances are equally spaced, as long as the quadratic Zeeman shift is negligible. Even a large quantum register can be calibrated in principle by determining just a single resonance splitting of any two neighboring ions.

In addition, the inhomogeneity of the magnetic field makes the equilibrium positions of the ions state dependent and thus creates a coupling between spin and motion [5, 51–53] which can be used for sideband cooling below the Doppler limit [54] and to create spin-motion entanglement [55]. Furthermore, the magnetic gradient creates an effective spin–spin coupling [35] which can be tuned globally [5] and locally [20, 56–58]. The spin–spin coupling can be used to implement conditional gates, and a CNOT gate has been demonstrated experimentally [5].

Fluctuations of the magnetic field introduce a diffusion of the state vector and thus lead to dephasing, usually on a millisecond timescale. Coherence times on a second scale can be recovered by using dressed states [59–61] which can be obtained by a continuous driving of the qubit transitions.

5.1 Coupling in an axial magnetic gradient

A spin flip of ion i between ground state $|g\rangle$ and excited state $|e\rangle$ with a magnetic field-dependent qubit splitting $E_e - E_g$ results in a change in the force δF_i experienced by the ion, given by

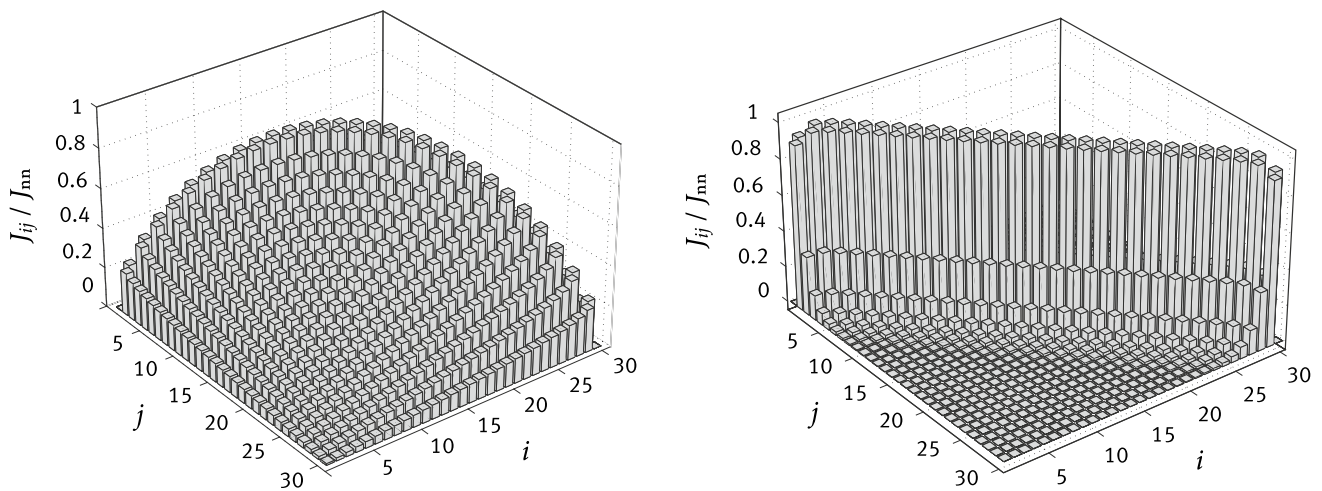


Fig. 18 *Left* effective spin–spin coupling between ion i and ion j for equidistant ions exposed to a homogeneous magnetic gradient. No mode tuning has been applied. The coupling is found to be largest in the string center, where the axial potential curvature is lowest, and is very different compared to couplings obtained by harmonic trapping. *Right* effective spin–spin coupling for same setup with an additional standing wave, effectively doubling the diagonal elements of the nor-

mal mode matrix. The nature of the coupling is dramatically altered, and the coupling is found to be predominantly next neighbor. The next-neighbor coupling strength reduces only slightly toward the ends for a string of 30 ions. As discussed in Sect. 4.2, the same normal mode matrix can be achieved for the transverse modes with an appropriately chosen radial confinement, thus yielding the same coupling pattern for a transverse gradient

$$\delta F_i = -\partial_z(E_e - E_g)|_{z=\bar{z}_i} \tag{42}$$

and all other entries of the force vector $\delta \mathbf{F}$ are zero. The normal mode matrix leads to a set of changed equilibrium positions

$$\Delta \bar{\mathbf{z}} = -\hat{K}^{-1} \delta \mathbf{F} \tag{43}$$

Ion j is shifted by the amount $\Delta \bar{z}_j$ and its energy level splitting changes by

$$\Delta E_j(i) = \hbar J_{ij} = \partial_z(E_e - E_g)|_{z=\bar{z}_j} \Delta \bar{z}_j \tag{44}$$

with the effective spin–spin coupling J_{ij} expressed as an angular frequency. For low magnetic fields, the Zeeman effect can be linearized and the lower and upper state energy of the qubit is given by

$$E_{g,e} = -g_{g,e} m_{g,e} \mu_B B \tag{45}$$

with the Landé-g-factors $g_{g,e}$, the Zeeman quantum numbers $m_{g,e}$, the Bohr magneton μ_B and the magnetic field B . If both states belong to the same hyperfine level, the spatial derivatives in Eqs. (42), (44) simplify to

$$\partial_z(E_e - E_g)|_{z=\bar{z}_i} = g \mu_B \partial_z B|_{z=\bar{z}_i} \tag{46}$$

for $|m_e - m_g| = 1$ for a magnetically sensitive dipole transition. The coupling between ion i and j is finally given by the matrix [56]

$$J_{ij} = -\hbar^{-1} g^2 \mu^2 \partial_z B|_{\bar{z}_i} \partial_z B|_{\bar{z}_j} (\hat{K}^{-1})_{ij} \tag{47}$$

Even though the normal mode matrix, and thus the coupling J_{ij} can be tuned, one cannot realize an arbitrary coupling matrix, as the coupling of the ions is dictated by the Coulomb interaction, and the normal mode matrix needs to fulfill Eq. (24).

For equidistant ions and no additional mode tuning potential, the lowest eigenvalue of \hat{K} approaches zero for $N \rightarrow \infty$ and the coupling matrix \hat{J} diverges with a maximum coupling growing proportionally to N . For a finite size of $N = 30$ ions and a homogeneous gradient $\partial_z B = \beta$, the coupling is well defined as shown in the left part of Fig. 18. The power of mode tuning, as described in Sect. 3.2, can be guessed from the right part in Fig. 18, where a homogeneous standing wave has been added. This yields a finite lowest eigenvalue and the coupling pattern acquires a very different shape. The unmodified normal mode matrix is always a symmetric Toeplitz matrix. For the alteration applied here, its inverse appears asymptotically to have Toeplitz shape, once the additional standing wave raises the lowest mode sufficiently. The coupling is then dominated by next-neighbor interaction and the next-neighbor coupling strength is almost uniform through the ion string, with finite size effects affecting a few ions at either end. For large separations $|i - j|$, the interaction decays as $|i - j|^{-3}$ as shown in Fig. 19. It can be seen that the decay is substantially different at smaller distances. The same coupling pattern can be obtained for a transverse gradient and an appropriately chosen radial confinement, as discussed in Sect. 4.2.

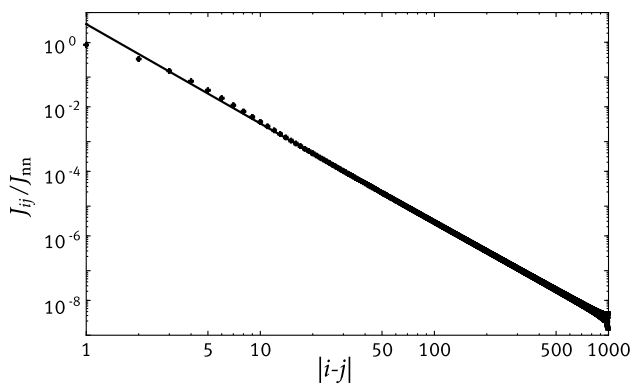


Fig. 19 Spin–spin coupling for a string of 1000 equally spaced ions. The coupling of all ions is plotted as a function of ion index difference which is proportional to the spatial distance. Vertical error bars (mostly visible only at the far right) indicate the scattering of coupling for a fixed distance and have been scaled by a factor of five, as they would have been invisible otherwise. A fit to the center points where end of chain effects are likely to be small by a function $\alpha_r|i - j|^r$ is indicated by a straight line. The coupling decays approximately inverse cubic as expected from the decay of the Coulomb interaction

Tailoring can become even more flexible by also shaping the spatial dependence of the gradient [62]. The coupling of harmonically trapped ions in axial and transverse gradients has been discussed in more detail in [20] for one- and two-dimensional crystals.

6 Creation of anharmonic potentials

The usage of segmented traps for moving, splitting and merging ion strings requires a determination of the voltages applied to electrode segments. An alternative strategy proposed in the context of quantum simulation is the optimization of electrode shapes to create microtraps in a desired pattern. In the following, we employ both approaches to create strings of approximately equidistant ions. The examples are calculated for surface traps with a five-wire design and a wire width of 50 μm .

6.1 Implementation in a segmented trap

If we want to create a string of equidistant ions, a common strategy for ion traps is to generate an axially homogeneous radial trapping potential with linear rf electrodes and to tweak the axial dependence of the effective potential by applying appropriate voltages on segmented dc electrodes obtained with an algorithm as, for example, the Tikhonov regularization (detailed in [63]). An alternative method based on the Schmidt decomposition is detailed in Appendix 3 and gives an intuitive approach, but does not allow for penalties to avoid oscillating solutions and high voltages.

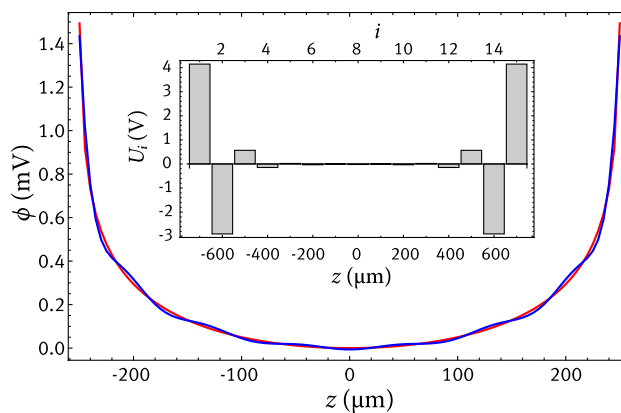


Fig. 20 Approximation of the anharmonic potential in a 15-segment five-wire surface trap to create an anharmonic potential for 100 equidistant ions with a separation of 5 μm , which is zoomed into the relevant region, where ions are stored. The desired potential is plotted in red and the optimized solution in blue. The segmentation generates deviations from the desired curve with a periodicity close to the segment width. The inset shows the voltages U_i applied to segment i

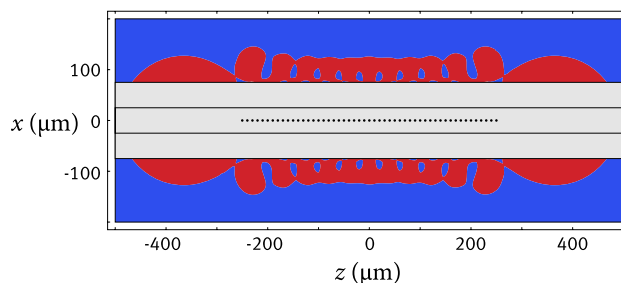


Fig. 21 Optimized surface trap electrode shaping to generate a string of 50 equidistant ions spaced by 10 μm : Gray areas are reserved for rf potentials and a central wire, which is set to dc ground. Red areas indicate electrodes set to +V, and blue areas are set to -1 V. The surface outside the plotted area is assumed to be set to dc ground. The ion-surface distance exceeds the inter ion distance by a factor of approximately 3.5 for this example

The Schmidt decomposition was used here to find voltages to approximate a potential which would trap an equidistant ion string of 100 ions, spaced by 5 μm . The geometry of the segments is identical to the one used in Appendix 3. The potential distribution in the relevant region is shown in Fig. 20 together with the required voltages. Deviations from the desired potential are still visible due to the coarse segmentation. The algorithm is not limited to 2-d problems and has been applied to obtain optimized voltages for the segmented 3-d trap described in [64].

6.2 Optimized electrode shapes

Instead of finding optimized voltages for a given electrode geometry, one can use numerical algorithms to design

optimized electrode shapes [65, 66], to generate the desired potential with a low number of voltages.

As an example, we optimize electrodes for trapping equidistant ions in a linear surface trap. As in the previous section, the rf trapping potential is realized by two rf wires separated by a ground wire of equal width. The rest of the surface is divided into pixels to partition the surface into electrodes on a potential of $\pm V$. The electric backward algorithm of the surface pattern package by Schmied [65, 66] was used to optimize the electrode shapes, and the result is shown in Fig. 21. When increasing the desired number of ions while keeping the separation constant, the algorithm moves the circular patterns at both ends further apart and adds more lobes between them.

7 Summary and outlook

In this work, we analyze trapping of linear isospaced ion crystals of arbitrary size, and the implications on required trapping potentials and axial and transverse dynamics. With additional potentials from standing waves, large crystals are feasible while maintaining a constant lowest normal mode, independent of crystal size. Obtaining the required trapping potential from a desired ion configuration is quite general and can be applied in other situations as well, also in higher dimensions.

The approach introduced here aims at the generation of large ion strings, and applications are expected for quantum simulations and QIS with transverse modes. The growing number of modes, the increasing mode density and the implications for cooling remain to be investigated. The transition to a zigzag might be interesting to analyze with such samples, as the conditions resemble more closely the homogeneous Kibble–Zurek mechanism.

Usually, ion traps are considered as a bottom up approach: Starting from an excellent degree of control over individual quantum systems (as high fidelity initialization, gates, read out), one attempts to scale up the system, ideally while maintaining that level of control, or investigating the scaling properties and obstacles added by the increased system size. Scaling up ion traps is argued always as possible in principle, but crystals forming two or higher-dimensional structures raise issues of stability, individual control and excess micromotion. In contrast, linear strings of chosen density and lowest mode frequency do not obviously struggle with these concerns. This type of trapping might thus allow for scaling experiments up to large ion crystals without compromising the degree of control on the single qubit level.

Acknowledgments We thank J. Jahnel, A. Böttcher, C. Wunderlich and the experimental quantum optics group in Siegen for fruitful discussions and proof reading. We acknowledge funding from the Bundesministerium für Bildung und Forschung (FK KIS0128), from the European Community’s Seventh Framework Programme (FP7/2007–2013) under Grant Agreement No. 270843 (iQIT), and from the European Metrology Research Program (EMRP), which is jointly funded by the EMRP participating countries within EURAMET and the European Union (EU).

Appendix 1: Polygamma function

The trigamma function $\psi^{(1)}(x)$ is a representative of the polygamma function $\psi^{(m)}(x)$ which relates to the ordinary gamma function $\Gamma(x)$ by

$$\psi^{(m)}(x) = \frac{d^m}{dx^m} \psi(x) = \frac{d^{m+1}}{dx^{m+1}} \ln \Gamma(x) \quad (47)$$

introducing the digamma function $\psi(x)$ as

$$\psi(x) = \psi^{(0)}(x) = \frac{\Gamma'(x)}{\Gamma(x)}. \quad (48)$$

The polygamma function $\psi^{(m)}(x)$ is related to the harmonic numbers $H_n^{(m)}$ by

$$\psi^{(m)}(z) = (-1)^{n+1} n! \left[\zeta(n+1) - H_{z-1}^{(n+1)} \right] \quad (49)$$

using the Riemann zeta function $\zeta(x)$.

Appendix 2: Normal mode matrix

We obtain normal modes from the linearized restoring forces provided by the external potential and the Coulomb forces between the ions [36]. The total potential energy of the ions is given as

$$E_{\text{tot}} = \sum_{i=1}^N \left(q\phi(\bar{z}_i) + \sum_{j<i}^N \frac{q^2}{4\pi\epsilon_0} \frac{1}{|\mathbf{r}_i - \mathbf{r}_j|} \right) \quad (50)$$

with $|\mathbf{r}_i - \mathbf{r}_j| = |z_i - z_j|$ for linear ion strings and can be computed using Eqs. (1), (5) for equidistant ion strings. For small excursion δ_i of ion i from its equilibrium position \bar{z}_i ,

$$z_i = \bar{z}_i + \delta_i, \quad (51)$$

the position dependence of the energy around the total minimum can be approximated as quadratic, and thus, the restoring force depends linearly on the excursions as

$$\mathbf{F} = m \ddot{\boldsymbol{\delta}} = -\hat{K} \boldsymbol{\delta}, \quad (52)$$

where \hat{K} is the Hessian matrix of the total energy

$$K_{ij} = \left. \partial_{z_i} \partial_{z_j} E_{\text{tot}} \right|_{z_i=\bar{z}_i, z_j=\bar{z}_j} = \left. \partial_{\delta_i} \partial_{\delta_j} E_{\text{tot}} \right|_{\delta_i=\delta_j=0} \quad (53)$$

and $\delta = (\delta_1, \dots, \delta_N)$ is the vector of excursions. The similarity to Hooke’s law suggests an ansatz where certain excursion patterns δ_n remain stable and just oscillate harmonically at angular eigenfrequency ν_n , as

$$\delta_n(t) = \delta_n(0) \cos(\nu_n t) \quad \text{and} \quad \ddot{\delta}_n(t) = -\nu_n^2 \delta_n(t) \quad (54)$$

which relates the equation of motion

$$-\hat{K} \delta_n = -m \nu_n^2 \delta_n \quad (55)$$

to an eigenvalue problem

$$\det(\hat{K} - \kappa_n \hat{1}) = 0 \quad (56)$$

with the eigenvalues $\kappa_n = m \nu_n^2$.

Appendix 3: Schmidt decomposition

The set of voltages which needs to be applied to a given electrode geometry to yield a desired trapping potential can be found with an algorithm as, for example, the Tikhonov regularization (detailed in [63]). In this section, we briefly introduce a simple alternative ansatz based on the Schmidt decomposition [67] which conveys an intuitive approach to the optimization. Similar to the Tikhonov regularization, we start with a set of basis solutions. Each solution is obtained by biasing the respective electrode, for example by 1 V, setting all other electrodes to ground and then calculating the resulting potential. Approximations can be found analytically for surface traps [68, 69] or the potentials are calculated numerically, e.g., by using the boundary element method [63]. Each possible potential distribution will now be composed as a weighted sum of all basis solutions.

The basis solutions can be viewed as vectors and the contribution of each basis vector to any given vector can be easily calculated, once the basis solutions are orthonormal. The Schmidt decomposition is a method to construct such a basis from any basis to start with [70]. The usage of the Schmidt decomposition in the context of QIP is discussed in [71]. For a set $V = \mathbf{v}_1, \dots, \mathbf{v}_N$ of linear independent vectors \mathbf{v}_i with the inner product $\mathbf{v}_k \mathbf{v}_k$, we can calculate an orthonormal basis $U = \mathbf{u}_1, \dots, \mathbf{u}_N$ with the vectors \mathbf{u}_i given by

$$\mathbf{u}_1 = \frac{\mathbf{v}_1}{\sqrt{\mathbf{v}_1 \mathbf{v}_1}} \quad \text{and} \quad \mathbf{u}_{i>1} = \sum_{k=1}^{i-1} \frac{\mathbf{v}_i \mathbf{u}_k}{\mathbf{u}_k \mathbf{u}_k} \mathbf{u}_k \quad (57)$$

The voltages required to construct a given potential are simply determined by calculating the projections of the desired potential onto the basis U using the inner product. If the basis vectors only span a subspace, the projections and the voltages obtained with this method yield the potential within the subspace which is closest to the desired one.

One will find, as with other procedures, that the reproduction of a desired potential distribution will be realized only approximately. Obviously, an arbitrary potential is parameterized by an infinite number of points in space (or alternatively Taylor coefficients), but only a finite number of boundary conditions can be satisfied by a finite number of electrodes. In addition, certain axial potentials may result in very large, probably alternating and experimentally impractical voltages. In such cases, more satisfying results can be obtained by using the Tikhonov regularization, which allows to introduce a penalty for high voltages [63].

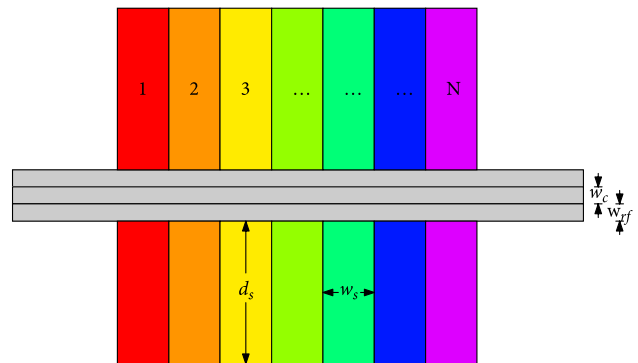


Fig. 22 Five-wire surface trap schematic, not to scale; the parameters chosen for the numerical simulations were: wire width $w_{\text{wire}} = w_c = w_{\text{rf}} = 50 \mu\text{m}$, segment width $w_s = 100 \mu\text{m}$, segment length $d_s = 1000 \mu\text{m}$

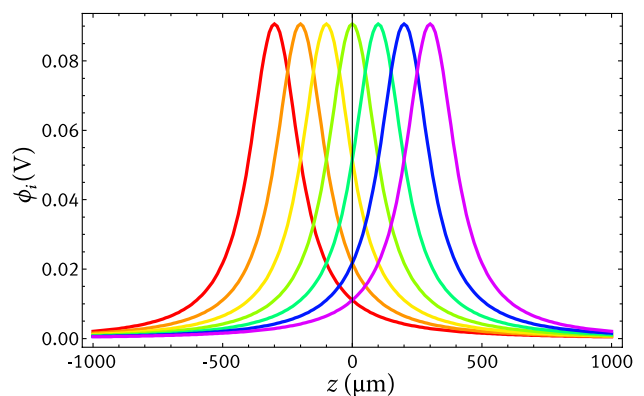


Fig. 23 Basis potentials of a planar symmetric five-wire seven-segment segmented trap with the layout and dimensions specified in Fig. 22. Basis solutions are obtained by applying 1 V to one segment, and all other segments are set to ground

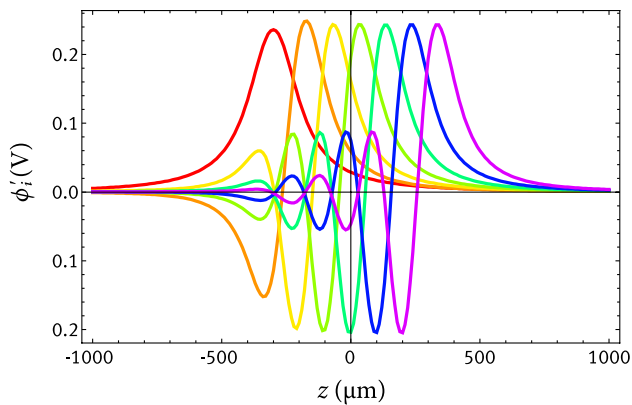


Fig. 24 Orthonormalized basis, created from the basis shown in Fig. 23. The first basis vector is, up to normalization unchanged, all others are reduced by their projection on the preceding vectors

We illustrate the Schmidt decomposition for a segmented symmetric five-wire planar trap where all wires have the width w_{wire} [72, 73]. For a five-wire trap and rectangular segment electrodes, in the limit of vanishing gaps between the electrodes, the potential distribution can be obtained analytically [68, 69] or numerically. The set of basis vectors V calculated for a geometry as shown in Fig. 22 and the trapping height $y_0 = \frac{\sqrt{3}}{2}w_{\text{wire}}$ are plotted in Fig. 23. The somewhat unintuitive orthonormal basis U obtained by applying Eq. (57) is displayed in Fig. 24. The Schmidt decomposition is used to find an approximation to a potential for the storage of an equidistant ion string in Sect. 6.1.

References

- J.I. Cirac, P. Zoller, Phys. Rev. Lett. **74**, 4091 (1995)
- D.J. Wineland, C. Monroe, W.M. Itano, D. Leibfried, B.E. King, D.M. Meekhof, J. Res. Natl. Inst. Stand. Technol. **103**, 259 (1998)
- H. Häffner, C.F. Roos, R. Blatt, Phys. Rep. **469**, 155 (2008)
- H.C. Nägerl, D. Leibfried, H. Rohde, G. Thalhammer, J. Eschner, F. Schmidt-Kaler, R. Blatt, Phys. Rev. A **60**, 145 (1999)
- A. Khromova, C. Piltz, B. Scharfenberger, T.F. Gloger, M. Johanning, A.F. Varón, C. Wunderlich, Phys. Rev. Lett. **108**, 220502 (2012)
- U. Warring, C. Ospelkaus, Y. Colombe, R. Jördens, D. Leibfried, D.J. Wineland, Phys. Rev. Lett. **110**, 173002 (2013)
- C. Piltz, T. Sriarunothai, A.F. Varón, C. Wunderlich, Nat. Commun. **5**, 4679 (2014)
- S. Crain, E. Mount, S. Baek, J. Kim, Appl. Phys. Lett. **105**, 181115 (2014)
- N. Navon, S. Kotler, N. Akerman, Y. Glickman, I. Almog, R. Ozeri, Phys. Rev. Lett. **111**, 073001 (2013)
- G.-D. Lin, S.-L. Zhu, R. Islam, K. Kim, M.-S. Chang, S. Korenblit, C. Monroe, L.-M. Duan, Europhys. Lett. **86**, 60004 (2009)
- W. Dür, H.-J. Briegel, J.I. Cirac, P. Zoller, Phys. Rev. A **59**, 169 (1999)
- L. Hartmann, B. Kraus, H.-J. Briegel, W. Dür, Phys. Rev. A **75**, 032310 (2007)
- L. Jiang, J.M. Taylor, K. Nemoto, W.J. Munro, R. Van Meter, M.D. Lukin, Phys. Rev. A **79**, 032325 (2009)
- A. Friedenauer, H. Schmitz, J.T. Glueckert, D. Porras, T. Schaetz, Nat. Phys. **4**, 757–761 (2008)
- M. Johanning, A.F. Varón, C. Wunderlich, J. Phys. B **42**, 154009 (2009)
- K. Kim, M.-S. Chang, S. Korenblit, R. Islam, E.E. Edwards, J.K. Freericks, G.-D. Lin, L.-M. Duan, C. Monroe, Nature **465**, 590–593 (2010)
- R. Gerritsma, B.P. Lanyon, G. Kirchmair, F. Zähringer, C. Hempel, J. Casanova, J.J. García-Ripoll, E. Solano, R. Blatt, C.F. Roos, Phys. Rev. Lett. **106**, 060503 (2011)
- S. Korenblit, D. Kafri, W.C. Campbell, R. Islam, E.E. Edwards, Z.-X. Gong, G.-D. Lin, L.-M. Duan, J. Kim, K. Kim, C. Monroe, New J. Phys. **14**, 095024 (2012)
- R. Blatt, C.F. Roos, Nat. Phys. **8**, 277 (2012)
- J. Welzel, A. Bautista-Salvador, C. Abarbanel, V. Wineman-Fisher, C. Wunderlich, R. Folman, F. Schmidt-Kaler, EPJ D **65**, 285 (2011)
- A. Bermudez, T. Schaetz, M.B. Plenio, Phys. Rev. Lett. **110**, 110502 (2013)
- H.J. Kimble, Nature **453**, 1023 (2008)
- D.L. Moehring, P. Maunz, S. Olmschenk, K.C. Younge, D.N. Matsukevich, L.-M. Duan, C. Monroe, Nature **449**, 68 (2007)
- S. Gerber, D. Rotter, M. Hennrich, R. Blatt, F. Rohde, C. Schuck, M. Almdendros, R. Gehr, F. Dubin, J. Eschner, New J. Phys. **11**, 013032 (2009)
- D. Hucul, I.V. Inlek, G. Vittorini, C. Crocker, S. Debnath, S.M. Clark, C. Monroe, Nat. Phys. **11**, 37 (2015)
- M. Albert, J.P. Marler, P.F. Herskind, A. Dantan, M. Drewsen, Phys. Rev. A **85**, 023818 (2012)
- B. Casabone, K. Friebe, B. Brandstätter, K. Schüppert, R. Blatt, T.E. Northup, Phys. Rev. Lett. **114**, 023602 (2015)
- D. Leibfried, M.D. Barrett, T. Schaetz, J. Britton, J. Chiaverini, W.M. Itano, J.D. Jost, C. Langer, D.J. Wineland, Science **304**, 1476 (2004)
- I.V. Inlek, G. Vittorini, D. Hucul, C. Crocker, C. Monroe, Phys. Rev. A **90**, 042316 (2014)
- K. Pyka, J. Keller, H.L. Partner, R. Nigmatullin, T. Burgermeister, D.M. Meier, K. Kuhlmann, A. Retzker, M.B. Plenio, W.H. Zurek, A. del Campo, T.E. Mehlstaebler, Nat. Commun. **4**, 2291 (2013)
- G. Birkel, S. Kassner, H. Walther, Nature **357**, 310 (1992)
- I. Waki, S. Kassner, G. Birkel, H. Walther, Phys. Rev. Lett. **68**, 2007 (1992)
- S. Fishman, G. De Chiara, T. Calarco, G. Morigi, Phys. Rev. B **77**, 064111 (2008)
- J.P. Home, D. Hanneke, J.D. Jost, D. Leibfried, D.J. Wineland, New J. Phys. **13**, 073026 (2011)
- C. Wunderlich, *Laser Physics at the Limits* (Springer, New York, 2002), pp. 261–271
- D.F.V. James, Appl. Phys. B **66**, 181 (1998)
- H. Landa, B. Reznik, J. Brox, M. Mielenz, T. Schaetz, New J. Phys. **15**, 093003 (2013)
- M. Mielenz, J. Brox, S. Kahra, G. Leschhorn, M. Albert, T. Schaetz, H. Landa, B. Reznik, Phys. Rev. Lett. **110**, 133004 (2013)
- S. Ulm, J. Roßnagel, G. Jacob, C. Degünther, S.T. Dawkins, U.G. Poschinger, R. Nigmatullin, A. Retzker, M.B. Plenio, F. Schmidt-Kaler, K. Singer, Nat. Commun. **4**, 2290 (2013)
- E. Shimshoni, G. Morigi, S. Fishman, Phys. Rev. Lett. **106**, 010401 (2011)
- P. Silvi, G. De Chiara, T. Calarco, G. Morigi, S. Montangero, Ann. Phys. **525**, 827–832 (2013)
- L. Hornekaer, N. Kjærgaard, A.M. Thommesen, M. Drewsen, Phys. Rev. Lett. **86**, 1994 (2001)

43. T.F. Gloger, P. Kaufmann, D. Kaufmann, M.T. Baig, T. Collath, M. Johanning, C. Wunderlich, Phys. Rev. A **92**, 043421 (2015)
44. M. Abramowitz, I.A. Stegun, *Handbook of Mathematical Functions with Formulas, Graphs, and Mathematical Tables* (Dover Publications, New York, 1972)
45. R.M. Gray, Found. Trends Commun. Inf. Theory **2**, 155 (2006)
46. C. Schneider, M. Enderlein, T. Huber, T. Schaetz, Nat. Photon. **4**, 772 (2010)
47. M. Enderlein, T. Huber, C. Schneider, T. Schaetz, Phys. Rev. Lett. **109**, 233004 (2012)
48. J.P. Schiffer, Phys. Rev. Lett. **70**, 818 (1993)
49. D.H.E. Dubin, Phys. Rev. Lett. **71**, 2753 (1993)
50. G.E. Astrakharchick, G. Morigi, G. De Chiara, J. Boronat, Phys. Rev. A **78**, 063622 (2008)
51. F. Mintert, C. Wunderlich, Phys. Rev. Lett. **87**, 257904 (2001)
52. F. Mintert, C. Wunderlich, Phys. Rev. Lett. **91**, 029902 (2003)
53. M. Johanning, A. Braun, N. Timoney, V. Elman, W. Neuhauser, C. Wunderlich, Phys. Rev. Lett. **102**, 073004 (2009)
54. S. Weidt, J. Randall, S.C. Webster, E.D. Standing, A. Rodriguez, A.E. Webb, B. Lekitsch, W.K. Hensinger, Phys. Rev. Lett. **115**, 013002 (2015)
55. K. Lake, S. Weidt, J. Randall, E.D. Standing, S.C. Webster, W.K. Hensinger, Phys. Rev. A **91**, 012319 (2015)
56. D. Mc Hugh, J. Twamley, Phys. Rev. A **71**, 012315 (2005)
57. H. Wunderlich, C. Wunderlich, K. Singer, F. Schmidt-Kaler, Phys. Rev. A **79**, 052324 (2009)
58. S. Zippilli, M. Johanning, S.M. Giampaolo, C. Wunderlich, F. Illuminati, Phys. Rev. A **89**, 042308 (2014)
59. N. Timoney, I. Baumgart, M. Johanning, A.F. Varón, M.B. Plenio, A. Retzker, Ch. Wunderlich, Nature **476**, 185 (2011)
60. S.C. Webster, S. Weidt, K. Lake, J.J. McLoughlin, W.K. Hensinger, Phys. Rev. Lett. **111**, 140501 (2013)
61. J. Randall, S. Weidt, E.D. Standing, K. Lake, S.C. Webster, D.F. Murgia, T. Navickas, K. Roth, W.K. Hensinger, Phys. Rev. A **91**, 012322 (2015)
62. P.J. Kunert, D. Georgen, L. Bogunia, M.T. Baig, M.A. Baggash, M. Johanning, C. Wunderlich, Appl. Phys. B **114**, 27 (2014)
63. K. Singer, U. Poschinger, M. Murphy, P. Ivanov, F. Ziesel, T. Calarco, F. Schmidt-Kaler, Rev. Mod. Phys. **82**, 2609 (2010)
64. D. Kaufmann, T. Collath, M.T. Baig, P. Kaufmann, E. Asenwar, M. Johanning, C. Wunderlich, Appl. Phys. B **107**, 935 (2012)
65. R. Schmied, J.H. Wesenberg, D. Leibfried, Phys. Rev. Lett. **102**, 233002 (2009)
66. R. Schmied, New J. Phys. **12**, 023038 (2010)
67. E. Schmidt, Math. Ann. **63**, 433 (1907)
68. M.H. Oliveira, J.A. Miranda, Eur. J. Phys. **22**, 31 (2001)
69. M.G. House, Phys. Rev. A **78**, 033402 (2008)
70. S. Roman, *Advanced Linear Algebra* (Springer, New York, 1992)
71. A. Ekert, P.L. Knight, Am. J. Phys. **63**, 415 (1995)
72. M.A. Rowe, A. Ben-Kish, B. Demarco, D. Leibfried, V. Meyer, J. Beall, J. Britton, J. Hughes, W.M. Itano, B. Jelenkovic, C. Langer, T. Rosenband, D.J. Wineland, Quantum Inf. Comput. **2**, 257 (2002)
73. J. Chiaverini, W.E. Lybarger, Phys. Rev. A **77**, 022324 (2008)